PIER C

Displacement Self-sensing Control of Permanent Magnet Assisted Bearingless Synchronous Reluctance Motor Based on BP Neural Network Optimized by Improved PSO

Jing Wang[1], Gai Liu[2, *], and Huangqiu Zhu[1, *]

[1]*School of Electrical and Information Engineering, Jiangsu University, Zhenjiang 212013, China*
[2]*School of Electrical and Control Engineering, Xuzhou University of Technology, Xuzhou 221018, China*

ABSTRACT: In order to solve the problems of low reliability, low integration, and high cost brought by mechanical sensors in the control system of permanent magnet-assisted bearingless synchronous reluctance motor (PMa-BSynRM), a displacement self-sensing method of the back propagation (BP) neural network left-inverse system under the optimization of an improved particle swarm algorithm is proposed. Firstly, the working principle of PMa-BSynRM is introduced, and the mathematical model of PMa-BSynRM is derived. Secondly, the suspension force model is established to prove the left reversibility of the PMa-BSynRM displacement subsystem on the basis of the observation principle of the left reversible system. Thirdly, the weights of BP neural network are optimized by using the improved particle swarm algorithm to avoid local optimum, and the final weights are obtained to complete the construction of the displacement self-detection control system. On this basis, velocity change and anti-interference simulations are conducted to prove the tracking performance of the displacement system. Finally, static suspension, velocity change and anti-interference experiments are executed which verify the accuracy and feasibility of the proposed displacement self-detection system.

1. INTRODUCTION

The synchronous reluctance motor (SynRM) differs from the permanent magnet synchronous motor in that it can still rotate when it has no excitation windings. The reluctance phenomenon was discovered through previous studies. In order to make full use of the d-q axis reluctance difference, reduce the excitation current, and increase the power factor, the permanent magnet assisted synchronous reluctance motor (PMa-SynRM) was born. PMa-SynRM inherits the significant advantages of synchronous reluctance motor and permanent magnet synchronous motor, such as large power density, high efficiency, wide speed range, light weight, and small size [1]. However, conventional motors face the problem of shortened service life due to mechanical bearing contact wear under high-speed operating conditions. The application of frictionless and wear-free permanent magnet-assisted bearingless synchronous reluctance motor (PMa-BSynRM) solves this problem. It also has a wide range of applications in high-purity fields such as chemical, pharmaceutical, biomedical and semiconductor industries due to its excellent performance of high speed, high precision, and maintenance-free [2–4].

The BSynRM is a nonlinear, strongly coupled MIMO system. For solving the coupling problem between two windings, [5] proposed a model-based state-space magnetic chain control method for a bearingless synchronous reluctance motor with two three-phase windings. It also has robustness in the case

of imprecise system parameters and rotor eccentricity. In [6], a dual-windings magnetic field orientation control scheme is proposed for the coupling problem of combined windings. Two different rotating coordinate systems are used to eventually superimpose the necessary phase currents to solve the problem. There are also adaptive parameter decoupling control methods [7] that can predict load variations and compensate for magnetic saturation. control scheme is proposed for the coupling problem of combined windings. There are also support vector machine decoupling control methods [8] and neural network decoupling control methods in intelligent algorithms [9].

Accurate detection of the radial displacement of the rotor is a key part of PMa-BSynRM stable suspension. Mechanical eddy current sensors are often used in traditional detection circuits to detect the displacement signal of the rotor. However, mechanical sensors are not suitable for high-speed and high-precision working environments due to high cost, large occupied area, and increased system structure. Sensorless displacement self-detection system has emerged.

Sensorless displacement technology through the acquisition of motor operation is easy to detect the non-displacement signal, according to the algorithm formula to derive displacement information to achieve the displacement sensor detection. Scholars have proposed a variety of displacement self-detection methods for bearingless motors. These include the classical high-frequency injection method [10–12], Kalman filter numerical simulation method [13], volumetric Kalman filter (CKF) rotor displacement prediction method under the optimization of Improved Quantum Particle Swarm Optimization

---

* Corresponding authors: Gai Liu (lg_just@163.com); Huangqiu Zhu (zhuhuang qiu@ujs.edu.cn).

(IQPSO) algorithm [14], and reciprocal inductive current detection rotor displacement estimation method [15]. Model Reference Adaptive System (MRAS) based rotor displacement estimation method depends on the accuracy of the model [16]. Further, the detection of rotor radial displacement is achieved using intelligent algorithms such as the least squares support vector machine [17]. This method has higher accuracy and good robustness, but the support vector machine theory is more complicated, difficult to train for large samples and long computation time.

In order to achieve the displacement-free sensor operation of PMa-BSynRM, this paper proposes to optimize the BP Neural Network (BPNN) using the improved particle swarm algorithm to adapt to the radial displacement of the system. The BPNN parameters are optimized using the IPSO algorithm to avoid falling into the local optimum and losing the global optimum solution, and to improve the convergence speed of the BPNN. The weights in the BPNN are mapped to particles in the IPSO algorithm, and the optimal initial weights are obtained by velocity update and position update to improve the speed and accuracy of the BPNN algorithm. The accuracy of the proposed displacement-free sensor model is verified by static suspension, velocity change, and sudden load simulation experiments.

2. WORKING PRINCIPLE AND MATHEMATICAL MODELING

2.1. Operation Principle of the PMa-BSynRM

The object of this paper is a permanent magnet-assisted bearingless synchronous reluctance motor (PMa-BSynRM) with a basic structure of 24 stator slots and 2 pairs of poles as shown in Fig. 1. The windings are two sets of torque windings and suspension force windings using a concentric winding structure, and the rotor adopts a three-layer magnetic barrier structure with inserted permanent magnet strips. The principle of torque generation of the PMa-BSynRM is the same as that of the conventional convex pole type reluctance motors based on the principle of minimum reluctance.
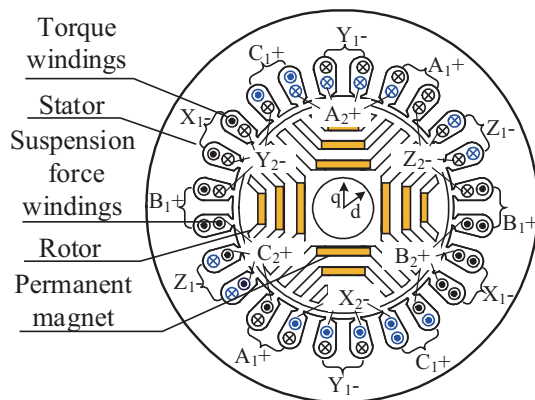

FIGURE 1. Basic structure of the PMa-BSynRM.

Figure 2 shows the schematic diagram of the suspension force generation. The suspension force windings N_B supplied with current generate the suspension force air gap magnetic
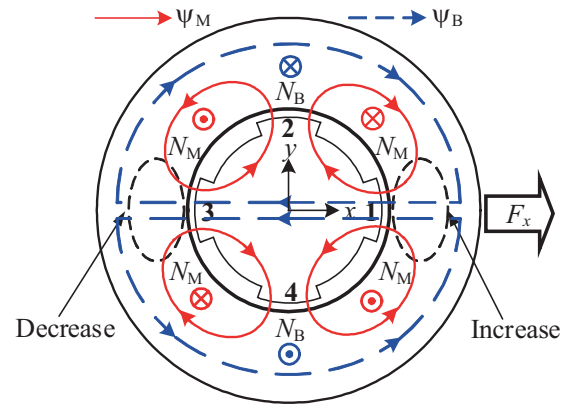

FIGURE 2. Mechanism of suspension force generation.

chain Ψ_B, and the torque windings N_M supplied with current and the permanent magnet inserted in the magnetic barrier generate the torque windings air gap magnetic chain Ψ_M. It can be seen in Fig. 2 that in the right region, the two fluxes are generated in the same direction, and the flux density increases, while in the left region, the two fluxes are in opposite directions, and the flux density decreases so that a suspension force F_x is generated in the positive direction along the x-axis. Similarly, to obtain a suspension force in the y-direction, it is sufficient to change the current phase of the suspension windings by $\pm 90°$. Therefore, by changing the phase and magnitude of the current in the suspension windings, suspension forces of different directions and amplitudes can be obtained.

2.2. Mathematical Model of the PMa-BSynRM

In the PMa-BSynRM model, the change of the rotor in radial displacement affects the magnetic chain of the suspension force and torque windings, and there is a coupling relationship between the windings current and the magnetic chain, and the magnetic chain equation of PMa-BSynRM can be expressed as:

$$
\begin{bmatrix} \psi_{Md} \\ \psi_{Mq} \\ \psi_{Bd} \\ \psi_{Bq} \end{bmatrix} = \begin{bmatrix} L_{Md} & 0 & M_d x_d & -M_d y_q \\ 0 & L_{Mq} & M_q y_q & M_q x_d \\ M_d x_d & M_q y_q & L_B & 0 \\ -M_d y_q & M_q x_d & 0 & L_B \end{bmatrix}
$$
$$
\begin{bmatrix} i_{Md} \\ i_{Mq} - i_0 \\ i_{Bd} \\ i_{Bq} \end{bmatrix} \tag{1}
$$

where Ψ_{Md} and Ψ_{Bd} are the d-axis air gap flux connection of the torque winding and the suspension force winding, respectively; Ψ_{Mq} and Ψ_{Bq} are the q-axis equivalent air gap flux connection of the torque winding and suspension force winding, respectively; L_{Md} and L_{Mq} are the self-sensing of the d- and q-axes of the torque winding, respectively; L_B is the self-perception of the suspension winding; M_d and M_q are the suspension constants; x_d and y_q are the d- and q-axis components of the radial displacement of the rotor. i_{Md} and i_{Bd} are the equivalent control current of the torque winding and the suspension force winding d-axis, respectively; i is the equivalent excitation current of the

permanent magnet defined in the negative direction of the q-axis; i_{Mq}, i_{Bq} are the q-axis equivalent control current of the torque winding and suspension force windings, respectively.

On the basic of the magnetic chain equation obtained from Equation (1), the deduced magnetic coenergy equation for the PMa-BSynRM is:

$$
\begin{aligned}
W_{\mathrm{m}} &= \frac{1}{2} \begin{bmatrix} i_{\mathrm{Md}} & i_{\mathrm{Mq}} - i_0 & i_{\mathrm{Bd}} & i_{\mathrm{Bq}} \end{bmatrix} \\
&\quad \cdot \begin{bmatrix} \psi_{\mathrm{Md}} & \psi_{\mathrm{Mq}} & \psi_{\mathrm{Bd}} & \psi_{\mathrm{Bq}} \end{bmatrix}^{\mathrm{T}} \\
&= \frac{1}{2}[L_{\mathrm{Md}}i_{\mathrm{Md}}^2 + L_{\mathrm{Mq}}(i_{\mathrm{Mq}} - i_0)^2 + L_{\mathrm{B}}(i_{\mathrm{Bd}}^2 + i_{\mathrm{Bq}}^2)] \\
&\quad + [M_{\mathrm{d}}i_{\mathrm{Md}}i_{\mathrm{Bd}} + M_{\mathrm{q}}(i_{\mathrm{Mq}} - i_0)i_{\mathrm{Bq}}]x_{\mathrm{d}} \\
&\quad - [M_{\mathrm{d}}i_{\mathrm{Md}}i_{\mathrm{Bq}} - M_{\mathrm{q}}(i_{\mathrm{Mq}} - i_0)i_{\mathrm{Bd}}]y_{\mathrm{q}}
\end{aligned} \tag{2}
$$

The magnetic coenergy W_{m} is deflected with respect to the radial displacements x_{d} and y_{q}, respectively, to obtain the suspension force component of the rotor in the d-q coordinate system as:

$$
\begin{bmatrix} F_{\mathrm{md}} \\ F_{\mathrm{mq}} \end{bmatrix} = \begin{bmatrix} \frac{\partial W_{\mathrm{m}}}{\partial x_{\mathrm{d}}} \\ \frac{\partial W_{\mathrm{m}}}{\partial y_{\mathrm{q}}} \end{bmatrix} = \begin{bmatrix} M_{\mathrm{d}}i_{\mathrm{Md}} & M_{\mathrm{q}}(i_{\mathrm{Mq}} - i_0) \\ M_{\mathrm{q}}(i_{\mathrm{Mq}} - i_0) & -M_{\mathrm{d}}i_{\mathrm{Md}} \end{bmatrix}
$$

$$
\begin{bmatrix} i_{\mathrm{Bd}} \\ i_{\mathrm{Bq}} \end{bmatrix} \tag{3}
$$

In addition, the magnitude of the unilateral magnetic pull force is directly proportional to the eccentric position of the rotor. The unilateral magnetic pull force can be written in the stationary two-phase α- and β-axis system as:

$$
\begin{bmatrix} F_{\mathrm{c}\alpha} \\ F_{\mathrm{c}\beta} \end{bmatrix} = \begin{bmatrix} k_{\mathrm{d}}i_{\mathrm{Md}}^2 + k_q(i_{\mathrm{Mq}} - i_0)^2 \end{bmatrix} \begin{bmatrix} x_{\mathrm{d}} \\ y_{\mathrm{q}} \end{bmatrix} \tag{4}
$$

where k_{d}, k_{q} are the eccentric displacement constants.

Based on Equation (3) and Equation (4), the complete mathematical model of the suspension force of PMa-BSynRM can be obtained as:

$$
\begin{aligned}
\begin{bmatrix} F_{\mathrm{B}\alpha}^* \\ F_{\mathrm{B}\beta}^* \end{bmatrix} &= \begin{bmatrix} F_{\mathrm{c}\alpha} \\ F_{\mathrm{c}\beta} \end{bmatrix} + \begin{bmatrix} F_{\mathrm{B}\alpha} \\ F_{\mathrm{B}\beta} \end{bmatrix} \\
&= \begin{bmatrix} k_{\mathrm{d}}i_{\mathrm{Md}}^2 + k_q(i_{\mathrm{Mq}} - i_0)^2 \end{bmatrix} \begin{bmatrix} x_{\mathrm{d}} \\ y_{\mathrm{q}} \end{bmatrix} \\
&\quad + \sqrt{M_{\mathrm{d}}^2 i_{\mathrm{Md}}^2 + M_{\mathrm{q}}^2 \left(i_{\mathrm{Mq}}^2 - i_0 \right)^2} \bullet
\end{aligned}
$$

$$
\begin{bmatrix} -\cos(2\omega t + \theta) & \sin(2\omega t + \theta) \\ \sin(2\omega t + \theta) & \cos(2\omega t + \theta) \end{bmatrix} \begin{bmatrix} i_{\mathrm{B}\alpha} \\ i_{\mathrm{B}\beta} \end{bmatrix} \tag{5}
$$

3. ANALYSIS OF THE LEFT-INVERTIBILITY OF THE DISPLACEMENT SUBSYSTEM

The left inverse is a basic concept in nonlinear control theory. It is used to observe the quantity of system variables that cannot be directly observed, just like observability in linear control theory. A class of multiple-input multiple-output (MIMO) nonlinear systems Ω is shown in the following Equation (6):

The general nonlinear system Ω can be expressed as:

$$
\begin{cases} \dot{x} = f(x, u) \\ y = h(x, u) \end{cases} \quad x(t_0) = x_0 \tag{6}
$$

where $u(t) = [u_1 \ldots u_q]^{\mathrm{T}}$ are the input variables of the system; $y(t) = [y_1 \ldots y_q]^{\mathrm{T}}$ are the Output variables of the system; $x = [x_1 \ldots x_n]^{\mathrm{T}} \in R^n$ are the state variables of the system; $x(t_0) = x_0$ are the initial state of the system.

Assume that the system Ω can be represented by a mapping operator λ in terms of its input-output relationship, the system can be represented as:

$$
y = \lambda u \tag{7}
$$

Suppose that corresponding to the above system, there exists system Π, with the same initial conditions as system Ω, then the system Π is expressed as:

$$
u^* = \xi y^* \tag{8}
$$

where u^* is the output variable of the system Π, y^* the input variable, and ξ the mapping operator.

If system Ω satisfies the condition $u = u^*$ and system Π satisfies the condition $y = y^*$, then the system Π is defined as the left-inverse system of the system Ω.

When Equation (6) contains an internal sensor system Z, the input is the direct observation variable x_{n}, and the output of the internal sensor system is the non-direct observation variable x_{i}. The input variable x_{n} can be expressed as:

$$
x_{\mathrm{n}} = f_{Z\Omega}(x_{\mathrm{i}}, \dot{x}_{\mathrm{n}}, \ddot{x}_n, \cdots, u) \tag{9}
$$

where $x = (x_{\mathrm{n}}, x_{\mathrm{i}})^{\mathrm{T}} \in \mathbf{R}^{\mathrm{n}}$ is the state variable.

If system Z exists, then x_{i} can be obtained, which can be expressed as:

$$
x_i = f_{Z\Pi}(x_{\mathrm{n}}, \dot{x}_n, \ddot{x}_n, \ldots, u, \dot{u}, \ddot{u}, \ldots) \tag{10}
$$

In order to realize the observation of the displacement, $x_i = [x_{\mathrm{d}}, y_{\mathrm{q}}]^{\mathrm{T}}$ is selected as the non-direct observed variable, and $x_n = [\psi_{\mathrm{Bd}}, \psi_{\mathrm{Bq}}]^{\mathrm{T}}$ is selected as the direct observed variable. Then the differential equations of the flux linkage of the suspension force windings are formulated as:

$$
\begin{bmatrix} \dot{\psi}_{B\mathrm{d}} \\ \dot{\psi}_{B\mathrm{q}} \end{bmatrix} = \begin{bmatrix} -\frac{R_{\mathrm{B}}}{L_{\mathrm{B}}} & f_{\mathrm{B}} \\ -f_{\mathrm{B}} & -\frac{R_{\mathrm{B}}}{L_{\mathrm{B}}} \end{bmatrix} \cdot \begin{bmatrix} M_{\mathrm{d}}x_{\mathrm{d}} & M_{\mathrm{q}}y_{\mathrm{q}} & L_{\mathrm{B}} & 0 \\ -M_{\mathrm{d}}y_{\mathrm{q}} & M_{\mathrm{q}}x_{\mathrm{q}} & 0 & L_{\mathrm{B}} \end{bmatrix}
$$

$$
\cdot \begin{bmatrix} i_{\mathrm{Md}} & i_{\mathrm{Mq}} - i_0 & i_{\mathrm{Bd}} & i_{\mathrm{Bq}} \end{bmatrix}^{\mathrm{T}} + \begin{bmatrix} u_{\mathrm{Bd}} & u_{\mathrm{Bq}} \end{bmatrix}^{\mathrm{T}} \tag{11}
$$

where f_{B} is the angular frequency of the magnetic field of the suspension force winding; R_{B} is the resistance of the suspension force winding; and u_{Bd}, u_{Bq} are the equivalent voltages of the d- and q-axes of the suspension force winding.

The corresponding Jacobi matrix correlation is determined as follows:

$$A(x) = \left(\frac{\partial (x_i, \dot{x}_i)}{\partial x_n} \right)$$

$$= \left(\left| \begin{matrix} -\frac{R_B}{L_B} & f_B \\ -f_B & -\frac{R_B}{L_B} \end{matrix} \right| \left| \begin{matrix} i_{Mg}M_d & (i_{Mq} - i_0)M_q \\ (i_{Mq} - i_0)M_q & -i_{Md}M_d \end{matrix} \right| \right) \quad (12)$$

The determinant of the Jacobi matrix is:

$$\det[A(x)] = -\left(\frac{R_B^2}{L_{Bd}^2} + f_B^2 \right)\left[i_{Md}^2 M_d^2 + (i_{Mq} - i_0)^2 M_q^2 \right] \neq 0 \quad (13)$$

Since $\det[A(x)] \neq 0$, it can be known that $A(x)$ is non-singular. The magnitude of the rank is equal to the non-directly observable quantity, and $\text{rank}[A(x)] = 2$, which indicates that there is a left inverse system of the constructed radial displacement subsystem $x_n = [\psi_{Bd}, \psi_{Bq}]^T$, and its left inverse system expression can be expressed as:

$$x_i = [x_d, x_q] = f_{Z\Pi}(x_n, \dot{x}_n, u) \quad (14)$$

4. IMPROVED PARTICLE SWARM OPTIMIZATION BP NEURAL NETWORK DISPLACEMENT LEFT INVERSE SYSTEM MODELING

4.1. BP Neural Network Algorithm

BPNN is a multi-layer forward structure network, which uses its advantages of accurately approximating nonlinear functions to fit the left inverse model of the displacement subsystem, thereby reducing calculation time and making up for the difficulty of establishing an accurate mathematical model. In this paper, a three-layer BPNN including input layer, hidden layer, and output layer is selected, and the structure is shown in the following Fig. 3.
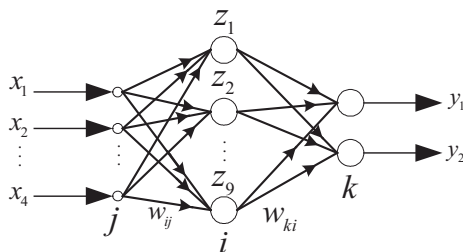
FIGURE 3. BP Neural Network structure diagram.

Each layer of BPNN is interpreted as:

Input Layer: the sample values are fed into the input vector of the implicit layer, which can be written for each node:

$$O_j^1 = x_j, \quad j = 1, 2, \ldots, 4 \quad (15)$$

where x_j is the input variable of the BPNN, and superscripts 1, 2, and 3 denote the input, hidden, and output layers, respectively.

The input and output of each node of the hidden layer can be written as:

$$h_i^2 = \sum_{i=1}^{9} w_{ij}O_j^1$$

$$O_i^2 = g_i(h_i^2 - \delta_i) \quad (16)$$

where w_{ij} is the connection weight between the j_{th} neuron in the input layer and the i_{th} neuron in the hidden layer; δ_i is the bias of the i_{th} neuron in the hidden layer; $g_i(x)$ is the activation function of the hidden layer, and the tanh function with high priority is used with the following expression:

$$g_i(x) = \frac{e^x - e^{-x}}{e^x + e^{-x}} \quad (17)$$

The inputs and outputs of each node of the output layer can be written as:

$$p_k^3 = \sum_{k=1}^{2} w_{ki}O_i^2$$

$$O_k^3 = g_k(p_k^3 - \delta_k) \quad (18)$$

where w_{ki} is the connection weight between the i_{th} neuron in the hidden layer and the k_{th} neuron in the output layer; δ_k is the bias of the k_{th} neuron in the output layer; and $g_k(x)$ is the activation function of the output layer, which uses a sigmoid function normalized to the output of each neuron with the following expression:

$$g_k(x) = \frac{1}{1 + e^{-x}} \quad (19)$$

In order to calculate the individual fitness values and observe the fitting accuracy, the following equation is given as the fitness function:

$$E_1 = \frac{1}{2}\sum_{i=1}^{N}(y_i - \hat{y}_i)^2 \quad (20)$$

where N is the number of training samples, y_i the actual output, and $\hat{y}_i$ the desired output.

4.2. Parameter Optimization Based on IPSO

BPNN algorithm is widely used in model prediction because of the advantage of its strong nonlinear fitting ability, but it is prone to the problem of falling into local extremes and losing the global optimal solution. NSGA-II has high computational complexity, lack of elite strategy, and other problems. Therefore, IPSO is proposed to optimize the BPNN. Based on the traditional particle swarm algorithm, the learning factor and inertia weights are improved to further improve the speed and accuracy of the system in searching the global optimum.

In the IPSO algorithm, each particle can be considered as a point in the solution space. Assuming that the target is searched in an M-dimensional space and there are n particles in the

group, x_i is the M-dimensional space position vector of the i_{th} particle. $P_{best}[i]$ and $g_{best}[i]$ denote the optimal position obtained by a single particle and the whole group, respectively, at the current position, and the velocity of the particles is denoted by v_i.

The iterative equation for the velocity and position of each particle is obtained as:

$$\begin{cases} v_{im}^{k+1} = wv_{im}^k + c_1 r_1 (p_{im} - x_{im}^k) + c_2 r_2 (p_{gm} - x_{im}^k) \\ x_{im}^{k+1} = x_{im}^k + v_{im}^{k+1} \end{cases}$$

(21)

where $i = 1, 2, \ldots n$, $m = 1, 2, \ldots M$, and k is the number of current iterations. r_1 and r_2 are random numbers between [0,1], which play the role of maintaining population diversity. Meanwhile, $v_{\min} \leq v_i \leq v_{\max}$, $x_{\min} \leq x_i \leq x_{\max}$. c_1, c_2 are the learning factors, and m is the inertia weights. The improved formula is as follows:

$$\begin{cases} c_1 = (c_{sta} - c_{end}) \frac{k_{\max} - k}{k_{\max}} + c_{end} \\ c_2 = 4 - c_1 \\ m = (m_{sta} - m_{end}) \frac{k_{\max} - k}{k_{\max}} + m_{end} \end{cases}$$

(22)

where $k_{\max}$ is the maximum number of iterations, and c_{sta} and c_{end} are the initial and final values of c_1. Set $0 < c_{sta} < c_{end} \leq 4$; c_{sta} and c_{end} are the initial and final values of the learning factor c_1. In the early stage, setting a larger c_1 and a smaller c_2 allows the particles to accelerate to a single extreme value. As the number of iterations increases, c_1 gradually decreases, and c_2 gradually increases, which accelerates the particle tracking group poles and speeds up the convergence speed; set $0.1 m_{end} < m_{sta} \leq 0.9$, generally take m_{sta} larger and m_{end} smaller to improve the global search ability.

Table 1 below shows the iteration speed and accuracy of the BP algorithm, PSO-BP algorithm, and IPSO-BP algorithm.

TABLE 1. The comparison of the three algorithms.

Algorithm	Number of hidden layer nodes	Mean number of iterations	Anticipation error	Mean CPU Time (μm)
BP	12	192	0.17	374
PSO-BP	11	46	0.01	197
IPSO-BP	9	34	0.001	131

We can see from Table 1 that the BPNN optimized by IPSO is greatly improved in terms of connection number, average iterations, and average CPU time, especially far better than the traditional BPNN, which indicates that the BP neural network optimized by IPSO has a good training effect.

4.3. Displacement Self-Sensing System Modeling

When using IPSO-BP to establish the displacement self-detection model, the initial values of BPNN weights w_{ij} and w_{ki} have an important influence on the model prediction effect. The Xavier method is first used to solve the initialization problem of IPSO weights. After determining the initial weights of IPSO, the weights of BPNN are

optimized by using IPSO. Each particle in IPSO represents the set of weights in BPNN, and the optimal particle is obtained by changing the velocity and position of the particle through the iterative optimization of IPSO. The optimal particle is assigned to BPNN to obtain the final weights. For PMa-BSynRM, the specific flowchart of the established IPSO-BP displacement self-sensing-based model is shown in Fig. 4:
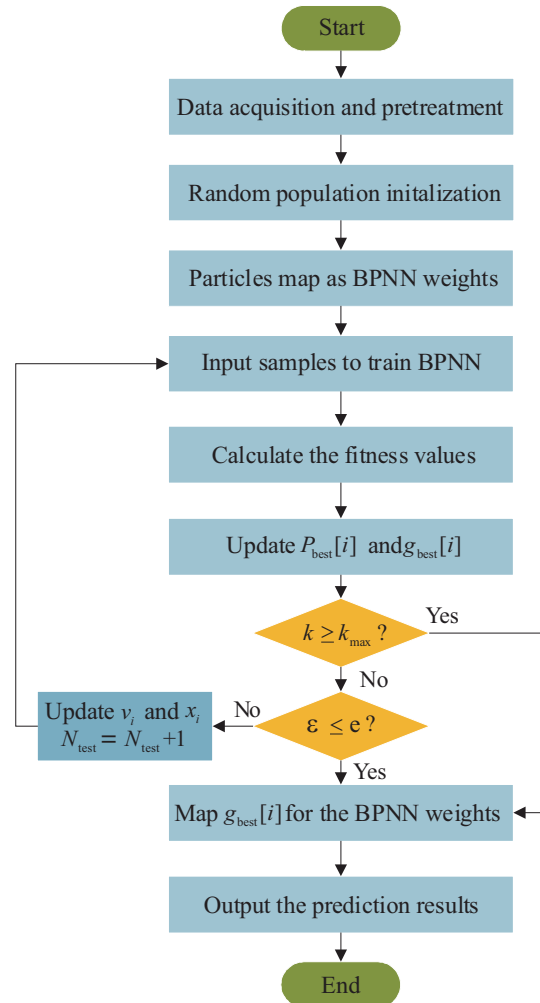
FIGURE 4. Flowchart of the displacement self-sensing model based on IPSO-BP.

1) Obtain the data set of displacement and related variables and perform data preprocessing.
2) Determine the parameters of the displacement self-detection model. Determine the neural network topology based on the neural network input and output data sets.
3) IPSO initialization. Set 80% of the samples as the training set. Set the initial IPSO weights $m_{sta} = 0.9$; set the final IPSO weights $m_{end} = 0.4$; set the initial value $c_{sta} = 3.4$ of the learning factor c_1, and the final value $c_{end} = 0.6$. Initialize the number of particles, where the number of particles is determined by the number of weights between the layers of the neural network.
4) Input and output data sets. Calculate the actual output displacement and predicted output displacement adjustment value.
5) Update the individual optimum and the population optimum by particle motion, and keep the particle velocity and position in the appropriate range.
6) When the maximum number of iterations is reached, or the error value between the actual displacement and the predicted dis-
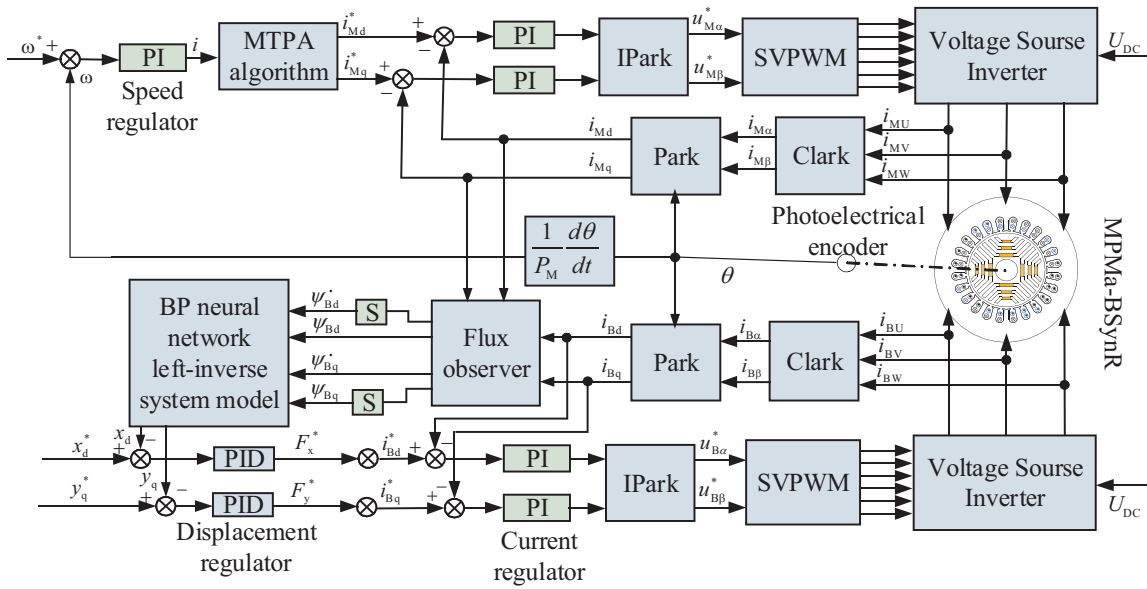
FIGURE 5. Displacement self-sensing control block diagram of the PMa-BSynRM.

placement is less than the minimum error requirement, output the optimal particle value, otherwise return to STEP (4).

7) Assign the optimal particle values to the weights of the BPNN; test the IPSO-BP displacement-based self-sensing model; and analyze the simulation results.

In this paper, the IPSO algorithm is used to optimize a three-layer BPNN, which has four input nodes with input vector $[x_n, \dot{x}_n] = [\psi_{Bd}, \psi_{Bq}, \dot{\psi}_{Bd}, \dot{\psi}_{Bq}]^T$, nine hidden layer nodes, and two output nodes with output vector $y_m = [x_d, y_q]^T$. The total sampling time is set to 1 s, and 1 ms is sampled once. A total of 1000 input vectors and 1000 output vectors are obtained. Of this, 80% of the data is used for training and 20% for testing.

In order to improve the accuracy and convergence speed of the model, the sample training and testing sets are normalized; the data of the samples are more concentrated; and the original data are converted to the range of [0,1] by using the normalization method of maximum-minimum normalization (MMN) with the following normalization formula:

$$norm(x) = \frac{x - \min(x)}{\max(x) - \min(x)} \qquad (23)$$

where $norm(x)$ represents the normalization of the results, and $\min(x)$ and $\max(x)$ are the minimum and maximum values of the input samples, respectively.

The IPSO algorithm is used to iteratively find the optimum for the normalized samples; the optimum value is assigned to the BPNN for training; and the trained data are back-normalized to produce the results predicted by the simulation. So far the PMa-BSynRM displacement self-sensing control system is established, as shown in Fig. 5.

5. SIMULATION TEST

5.1. Algorithm Optimization

MATLAB was used to compare and analyze the IPSO algorithm and PSO algorithm. Set the overall sample size to 100; the maximum number of iterations is 80 times; the particle velocity range is in $[-1,1]$;

and the particle position range is in $[-5,5]$. Map the BPNN weights to particles. The optimized BPNN weights are shown below:

$$w_{ij} = \begin{bmatrix} 1.3411 & 4.5708 & 4.0712 & 0.3624 \\ -0.2389 & -0.2891 & -1.0643 & 4.5946 \\ 2.6532 & 0.9645 & 1.9909 & -0.3913 \\ 0.8933 & 0.2420 & -0.5511 & 1.4846 \\ 1.9368 & 2.9126 & 0.7412 & 0.9513 \\ -0.3275 & 1.1573 & 1.4521 & 1.1076 \\ 0.7061 & -0.4663 & 2.0684 & -1.0755 \\ 1.3509 & 1.7328 & 3.0466 & 3.9666 \\ 0.5524 & 1.2990 & -0.5387 & 0.5615 \end{bmatrix}$$

$$w_{ki} = \begin{bmatrix} 0.3149 & -1.4260 \\ 1.8060 & 2.2702 \\ -0.7355 & 0.0479 \\ -1.5227 & -0.4758 \\ 2.0483 & 1.8220 \\ -3.1249 & -0.5845 \\ 0.7624 & -0.9886 \\ 0.9562 & 0.1915 \\ 0.3552 & 1.0336 \end{bmatrix}$$

The fitness value curves of IPSO are shown in Fig. 6. It can be seen that the standard PSO algorithm minimizes the fitness value and starts to converge in the 48th generation with a fitness value of 0.00789, whereas the IPSO algorithm minimizes the fitness value and starts to converge in the 39th generation with a fitness value of 0.000688. It can be seen that the IPSO algorithm has higher fitting accuracy and faster convergence speed than the standard PSO algorithm.

5.2. Speed Variation Simulation

Due to the gravity of the rotor, the initial displacements of the rotor are set to $x = 0$ mm and $y = -0.24$ mm, respectively. The rated speed is 5000 r/min, and the control period of the system is 0.1 ms. When the rotor speed rises to 5 000 r/min, the rotational speed diagram is shown in Fig. 7. The displacement fitting curve is shown in Fig. 8. The displacement fitting error is shown in Fig. 9. The actual values in
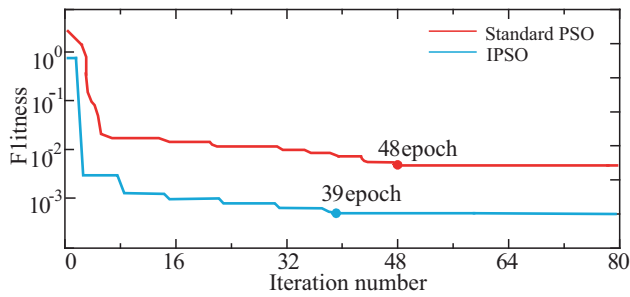
194

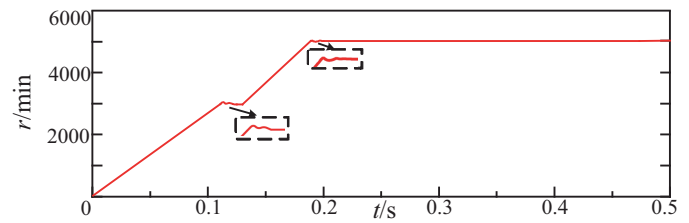**FIGURE 6.** Fitness curves of the IPSO and PSO.

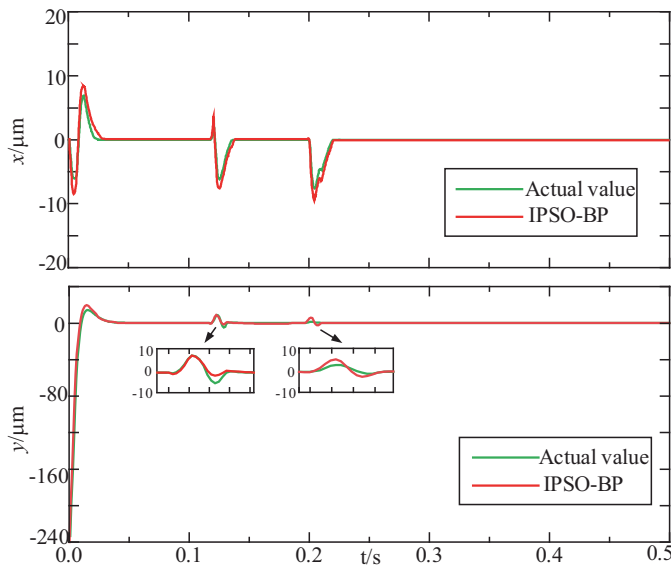**FIGURE 7.** Waveform diagram of rotor acceleration.

FIGURE 8. Rotor displacement diagram in the x- and y-directions.
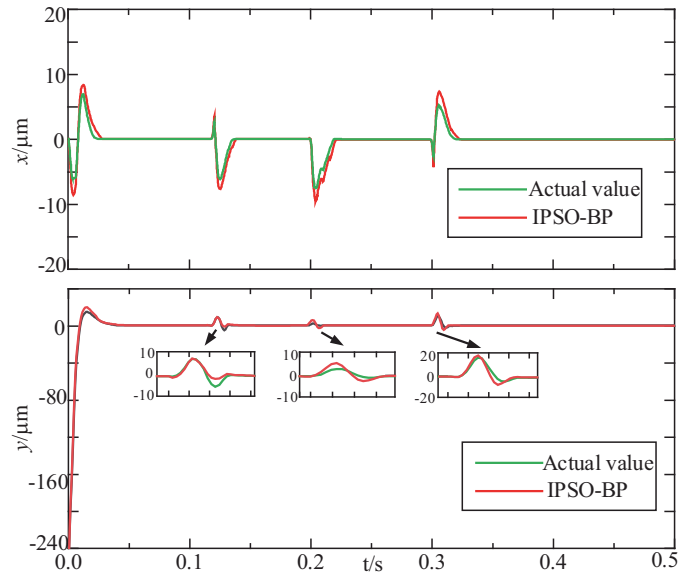

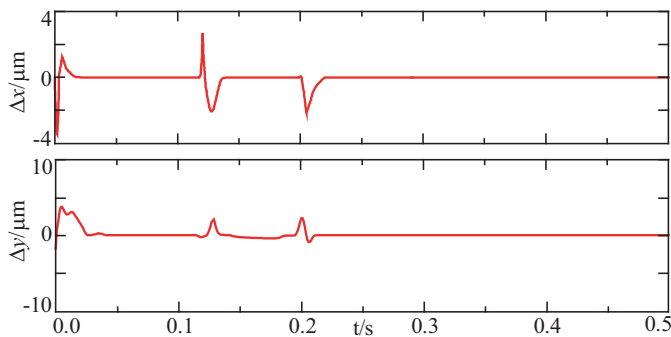**FIGURE 10.** Rotor displacement diagram in the x- and y-directions.

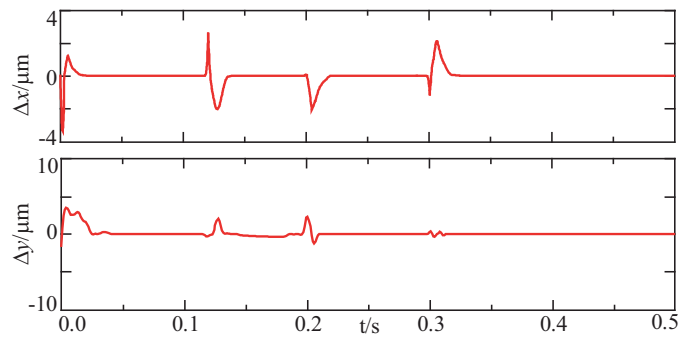**FIGURE 9.** Differential displacement of the rotor in the x- and y-directions.

FIGURE 11. Differential displacement of the rotor in the x- and y-directions.

the x-direction and y-direction are 7 μm and 18 μm, respectively. At the beginning, the rotor is accelerated to 3,000 r/min after 0.12 s. As shown in Fig. 8, the maximum magnitudes of the actual values in the x- and y-directions are 7 μm and 18 μm; the maximum magnitudes of the IPSO-BP in the x- and y-directions are 8 μm and 22 μm, respectively; and the speed stabilizes at 3 000 r/min after 0.14 s. The maximum magnitudes of the actual values in the x- and y-directions are 7 μm and 18 μm, and the maximum magnitudes of the IPSO-BP in the x- and y-directions are 8 μm and 22 μm, respectively. The maximum magnitudes of the actual values in the x- and y-directions are

7 μm and 4 μm, and the maximum magnitudes of the IPSO-BP in the x- and y-directions are 9 μm and 6 μm, respectively. From the analysis of the above data, the fitting result of IPSO-BP generally agrees with the actual results.

5.3. Anti-Interference Simulation

After the rotor is stabilized in suspension, a 35N y-axis positive impulse disturbance force is added at 0.3 s. The waveforms of the radial displacements in the x- and y-directions are shown in Fig. 10, and the
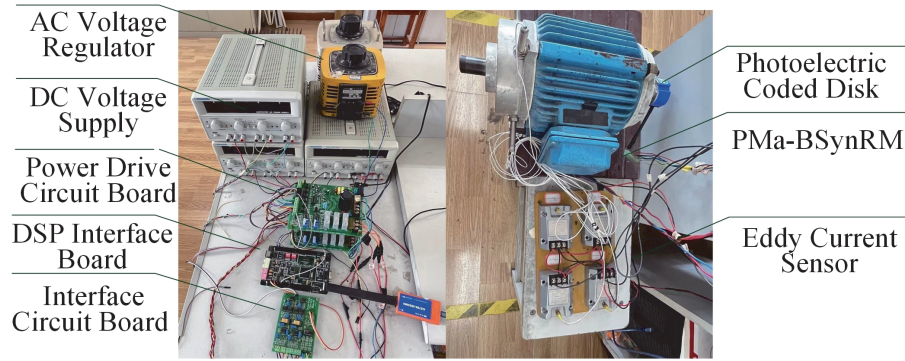
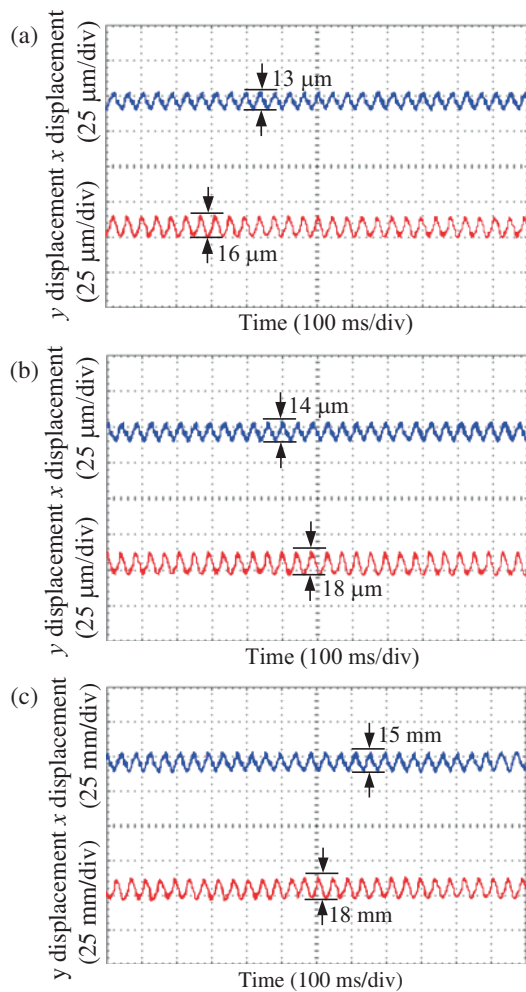**FIGURE 12**. The experimental platform of PMa-BSynRM.

FIGURE 13. Displacement waveform with rotor stable suspension at 3000 r/min. (a) The eddy current sensor. (b) IPSO optimized BPNN. (c) Improved NSGA-II optimized LSSVM.

FIGURE 14. Displacement waveform of the rotor accelerating from 3000 r/min to 5000 r/min. (a) The eddy current sensor. (b) IPSO optimized BPNN. (c) Improved NSGA-II optimized LSSVM.

displacement fitting errors are shown in Fig. 11. The maximum magnitudes of the real values in the x- and y-directions are 6 μm and 17 μm, respectively, and the maximum magnitudes of the IPSO-BP in the x- and y-directions are 8 μm and 18 μm, respectively. It can be seen that under the application of the interference force, the IPSO-BP fitting is effective, and it is able to change in real time along with the change of the real values. It has a good tracking performance.
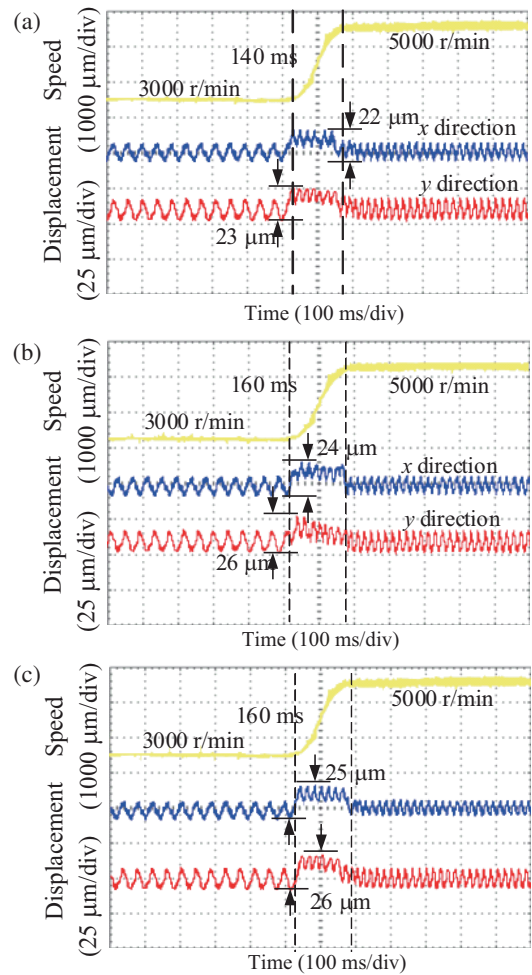
It is capable of tracking and predicting the displacement of the suspension system without using mechanical displacement sensors.

6. EXPERIMENT VALIDATION

The digital experimental platform of the PMa-BSynRM is shown in Fig. 12. It mainly includes PMa-BSynRM, digital signal processor

(DSP), inverter, PC host, optoelectronic encoder disk, oscilloscope, etc. In this paper, the DSP is used to realize the acquisition and processing of the experimental data, and the VB6.0 software is used to develop the man-machine integrated interactive interface. In the experiment, BPNN is offline. The PMa-BSynRM uses an auxiliary mechanical bearing with a clearance of 0.25 mm to cope with the unbalanced vibrations generated.

The main specifications and parameters of the platform are shown in Table 2.

TABLE 2. Parameters and description of the experimental platform.

Parameters	Values	Parameters	Values
n (r/min)	5 000	U_N (V)	220
δ_0 (mm)	0.25	ψ_0 (Wb)	0.0359
P_N (kW)	1.1	N_M/N_B	72/24
P_M/P_B	2/1	K_m	1.338
m (kg)	1.6	PM material	NdFeB
L_{SI}/L_{SO} (mm)	80/130	L_M (mm)	90
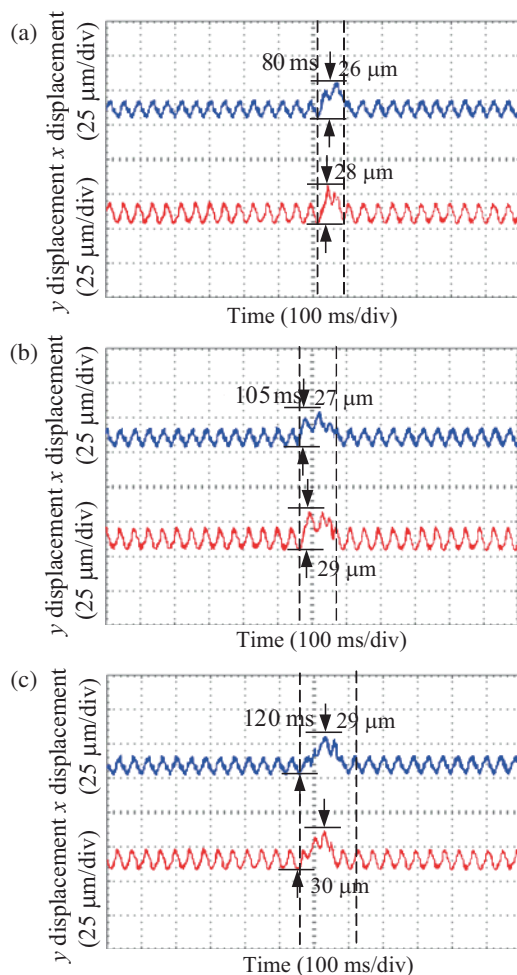
FIGURE 15. Displacement waveform of disturbing force applied in the y direction. (a) The eddy current sensor. (b) IPSO optimized BPNN. (c) Improved NSGA-II optimized LSSVM.

6.1. Static Suspension Experiment

The experimental waveforms of the radial displacement of the rotor in the x- and y-directions are shown in Fig. 13 when the rotor speed reaches 3000 r/min, and the suspension is stabilized. The eddy current sensor has a maximum displacement of 13 μm in the x-direction and 16 μm in the y-direction. The IPSO-BPNN has a maximum displacement of 15 μm in the x-direction and 18 μm in the y-direction. The improved NSGA-II optimized LSSVM has a maximum displacement of 15 μm in the x-direction and 18 μm in the y-direction. According to the experimental results, it can be seen that the proposed method has a good displacement fit and can be stably suspended.

6.2. Speed Variation Experiment

When the speed is accelerated from 3 000 to 5 000 r/min, the displacement waveforms in the x- and y-directions are shown in Fig. 14. The eddy current sensor has a maximum displacement of 22 μm in the x-direction and 23 μm in the y-direction, and the recovery time is 140 ms. The IPSO-BPNN has a maximum displacement of 24 μm in the x-direction and 26 μm in the y-direction, and the recovery time is 160 ms. The improved NSGA-II optimized LSSVM has a maximum displacement of 25 μm in the x-direction and 26 μm in the y-direction, and the recovery time is 160 ms. Compared with the LSSVM optimized by improved NSGA-II displacement self-detection method, the proposed method has better displacement accuracy and the same recovery time. From the data analysis, it can be seen that the proposed displacement self-sensing method can achieve a stable suspension of the rotor when the rotor accelerates and has good tracking performance.

6.3. Suspension Force Load Experiment

When the rotor is steadily suspended at 3000 r/min, an impulsive interference force of 35 N is added to the shaft using a spring dynamometer. Due to the presence of coupling, the successive interference forces result in fluctuations in the x- and y-directions. The radial displacement waveform when the rotor is disturbed in the y-direction is shown in Fig. 15. The eddy current sensor has a maximum displacement of 26 μm in the x-direction and 28 μm in the y-direction, with an recovery time of 80 ms. The IPSO-BPNN has a maximum displacement of
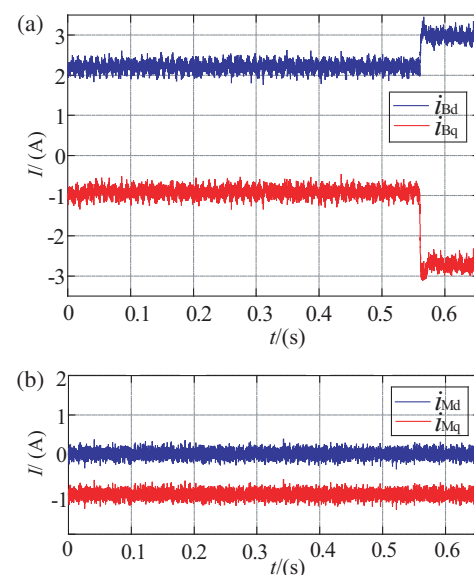
FIGURE 16. The d-q axis current in BPNN optimized by IPSO. (a) The d-q axis current of suspension force winding. (b) The d-q-axis current of torque winding.

27 μm in the x-direction and 29 μm in the y-direction, with a recovery time of 105 ms. The improved NSGA-II optimized LSSVM has a maximum displacement of 29 μm in the x-direction and 30 μm in the y-direction, with a recovery time of 120 ms. It can be seen from the analysis of the above data that the method proposed in this paper ensures the fitting accuracy and has good response recovery capability and tracking performance. The experimental results show that the proposed method has good dynamic characteristics and verifies the robustness of the system.

Figure 16 shows the current waveform patterns of the d- and q-axis of the BPNN optimized by IPSO. Fig. 16(a) is the d- and q-axis current waveform diagram of the suspension force winding. The interference force is introduced at 0.55 s to change the winding current of the suspension force. The amplitude of the suspended force winding current i_{Bd} oscillation changes from 2.45 A to 3.25 A, and the i_{Bq} oscillation amplitude of the suspended force winding changes from -1.1 A to -2.6A. Fig. 16(b) shows the d- and q-axis current wave pattern of the torque winding. The torque winding current i_{Md} oscillation amplitude is stabilized at 0.1 A, and the i_{Mq} oscillation amplitude of the torque winding is stabilized at 1.1 A.

7. CONCLUSION

Aiming at the problems of high cost and low reliability brought by mechanical displacement sensors to PMa-BSynRM, in this paper, a displacement self-sensing method is proposed, and the displacement curve of the rotor is fitted by the IPSO-BPNN method

1) In the simulation and experiment, the displacement self-sensing method can realize the rotor displacement detection under the conditions of static and stable suspension, speed change, and external disturbance force, with small accuracy error and good estimation effect.

2) It also has good rotor displacement tracking performance during the PMa-BSynRM startup phase due to the gravity of the rotor.

3) The displacement detection of the left inverse of the BP Neural Network, which does not depend on the model and parameters of the system, has good tracking performance and good anti-interference performance.

REFERENCES

[1] Xu, M., G. Liu, Q. Chen, J. Ji, and W. Zhao, "Design and optimization of a fault tolerant modular permanent magnet assisted synchronous reluctance motor with torque ripple minimization," *IEEE Transactions on Industrial Electronics*, Vol. 68, No. 9, 8519–8530, Sep. 2021.

[2] Hua, Y., H. Zhu, M. Gao, and Z. Ji, "Multiobjective optimization design of permanent magnet assisted bearingless synchronous reluctance motor using NSGA-II," *IEEE Transactions on Industrial Electronics*, Vol. 68, No. 11, 10 477–10 487, Nov. 2021.

[3] Sokolov, M., W. Gruber, S. E. Saarakkala, and M. Hinkkanen, "Modeling of a bearingless synchronous reluctance motor with combined windings," in *2019 IEEE Energy Conversion Congress and Exposition (ECCE)*, 7084–7090, Baltimore, MD, USA, 2019.

[4] Ji, Z., H. Zhu, Y. Xu, and M. Wu, "Optimization design of permanent magnet assisted single winding bearingless synchronous reluctance motor," *IEEE Transactions on Applied Superconductivity*, Vol. 30, No. 4, 1–5, Jun. 2020.

[5] Saarakkala, S. E., M. Sokolov, M. Hinkkanen, J. Kataja, and K. Tammi, "State-space flux-linkage control of bearingless synchronous reluctance motors," in *2016 IEEE Energy Conversion Congress and Exposition (ECCE)*, 1–8, Milwaukee, WI, USA, Sep. 2016.

[6] Gruber, W. and S. Silber, "Dual field-oriented control of bearingless motors with combined winding system," in *2018 International Power Electronics Conference (IPEC-Niigata 2018-ECCE Asia)*, 4028–4033, Niigata, Japan, May 2018.

[7] Kong, X. and L. Wang, "An adaptive parameter decoupling control method for bearingless synchronous reluctance motor," in *Proceeding of the 11th World Congress on Intelligent Control and Automation*, 4572–4576, Shenyang, China, Jun. 2014.

[8] Feng, D., L. Zhu, X. Diao, and H. Zhu, "Decoupling control of bearingless synchronous reluctance motor based on support vector machines inverse system," in *Proceedings of the 32nd Chinese Control Conference*, 547–551, Xi'an, China, 2013.

[9] Wang, Y., L. Cao, D. Feng, X. Diao, and H. Zhu, "Decoupling control based on neural network inverse for bearingless synchronous reluctance motor," in *Proceedings of the 31st Chinese Control Conference*, 3291–3295, Hefei, China, Jul. 2012.

[10] Zhang, Y., Y. Wang, C.-G. Zhang, and W.-J. Hao, "General analysis of combinations of high frequency injected auxiliary coils in displacement sensorless control," in *2021 IEEE 4th Student Conference on Electric Machines and Systems (SCEMS)*, 1–7, Huzhou, China, 2021.

[11] Nian, H., Y. Quan, and J. Li, "Rotor displacement sensorless control strategy for PM type bearingless motor based on the parameter identification," in *2009 International Conference on Electrical Machines and Systems*, 1–5, Tokyo, Japan, 2009.

[12] Tang, Q., A. Shen, X. Luo, and J. Xu, "PMSM sensorless control by injecting HF pulsating carrier signal into ABC frame," *IEEE Transactions on Power Electronics*, Vol. 32, No. 5, 3767–3776, May 2017.

[13] Tan, C., H. Wang, and Y. Wang, "Rotor eccentricity compensation of bearingless switched reluctance motors based on extended kalman filter," in *2019 12th International Symposium on Computational Intelligence and Design (ISCID)*, 111–115, Hangzhou, China, Dec. 2019.

[14] Sun, J. and H. Zhu, "Self-sensing technology of rotor displacement for six-pole radial active magnetic bearing using improved quantum particle swarm optimized cubature kalman filter," *IEEE Journal of Emerging and Selected Topics in Power Electronics*, Vol. 10, No. 3, 2881–2889, Jun. 2022.

[15] Tera, T., Y. Yamauchi, A. Chiba, T. Fukao, and M. A. Rahman, "Performances of bearingless and sensorless induction motor drive based on mutual inductances and rotor displacements estimation," *IEEE Transactions on Industrial Electronics*, Vol. 53, No. 1, 187–194, Feb. 2006.

[16] Nian, H., Y.-K. He, L. Huang, and H. Ying, "Sensorless operation of an inset PM bearingless motor implemented by the combination approach of MRAS and HF signal injection," in *2006 6th World Congress on Intelligent Control and Automation*, Vol. 2, 8163–8167, Dalian, 2006.

[17] Zhu, H. and Y. Shi, "Displacement self-sensing control of permanent magnet assisted bearingless synchronous reluctance motor based on least square support vector machine optimized by improved NSGA-II," *IEEE Transactions on Industrial Electronics*, Vol. 71, No. 2, 1201–1211, Feb. 2024.